Survey of Electronic and Local Structural Properties of $Cd_{1-x}Co_xSe_{1-y}Te(S)_y$ by XAFS

Ivana Radisavljević[1*], Nikola Novaković[1], Heinz–Eberhard Mahnke[2], Nebojša Romčević[3],
Miodrag Mitrić[1], Bojana Kuzmanović[1], and Nenad Ivanović[1]

[1]*Institute of Nuclear Sciences "Vinča" – National Institute of the Republic of Serbia,*
University of Belgrade, P.O. Box 522, 11001 Belgrade, Serbia
[2]*Helmholtz–Zentrum Berlin für Materialien und Energie GmbH D–14109 Berlin, Germany*
[3]*Institute of Physics – National Institute of the Republic of Serbia, University of Belgrade*
Pregrevica 118, 11000 Belgrade, Serbia

As an extension of our previous studies of multi–component semiconductors doped with magnetic impurities, this paper gives a comprehensive insight into electronic and local structure of crystalline semiconductors $Cd_{0.98}Co_{0.02}Se$, $Cd_{0.98}Co_{0.02}Se_{0.9}S_{0.1}$ and $Cd_{0.98}Co_{0.02}Se_{0.9}Te_{0.1}$. Detailed characterization of Co and Se local environment and overall influence of Co and S(Te) (co)doping on the host crystal structure has been obtained by X–ray absorption fine structure (XAFS) technique and electronic structure calculations. Important structural information on bond lengths and disorder parameters were extracted from the extended region of the absorption spectra, while the relationships between electronic and local structures were determined from the characteristic features appearing in the near–edge spectral region. The influence of various structural defects on local electronic properties, charge transfer and atomic interactions has been studied by theoretical modeling of XAFS spectra and calculations of local density of electronic states. The obtained findings offer possible means for improvement and extension of the practical application of CdSe–based materials by adjusting the details of their electronic structure.

Keywords: semiconductors, electronic structure, defects, XAFS.

1. Introduction

Owing to a broad range of stable stoichiometric crystalline systems with high absorption coefficient and direct energy gap (E_g) covering the ultraviolet and visible light region[1–3], multinary cadmium chalcogenides suitable for solar energy harvesting are an enduring subject of research interest[4]. At present, cadmium tellurides and sulfides are among the most promising photovoltaic materials for the fabrication of low cost and highly efficient solar cells[5]. The ability to relatively easily adjust the type of conductivity (n or p) and to optimize the E_g width makes the CdSe–based materials suitable also for various photocatalytic and optoelectronic applications[6]. The performances of these materials can be further improved and extended by doping with 3d transition metals (TM), especially Co, a shallow donor impurity[7] which effectively captures excited electrons[8].

Cadmium chalcogenides belong to II–IV semiconductor family with tetrahedrally coordinated wurtzite or zinc–blende crystal structure[9,10]. Although tetrahedral coordination is formed as a result of the sp^3 covalent bonding, the chemical bonds in Cd chalcogenides also have a substantial polar (ionic) contribution. Both polar and covalent contributions to bonding decrease with the atomic number of chalcogen ($CdS \rightarrow CdSe \rightarrow CdTe$), but since the polar contribution decreases much faster, the net effect is manifested as a relative increase of the covalent contribution[11,12]. This complex nature of bonding affects the essential material properties (lattice parameter, bulk modulus, cohesive energy, enthalpy of mixing, position of the band edges, E_g width, band offsets, optical bowing coefficient, …), which are reflected in a wide range of their optical characteristics[7,13–16]. In TM–doped II–IV semiconductors, delocalized TM $4s^2$ electrons are directly involved in tetrahedral bonding, while localized 3d–4s hybrid states interact with sp–bands of the host crystal[17]. The extent of s–d and p–d orbital mixing largely depends on the electronic structure of TM ion and its local coordination environment. Partially occupied TM 3d shell is subjected to crystal field splitting[18,19], and it is therefore sensitive to any distortion of the host crystal structure. In addition to distortions caused by native defects[20], structural disorder in multi–component cadmium chalcogenides is also likely to originate from the site occupation and the nearest neighbor preferences[10,21–24]. A deeper understanding of these atomic–scale effects would be beneficial in terms of both exploitation and future design of Cd chalcogenide materials, as it could shed light on many closely related phenomena and processes (e.g. doping limit, nature of impurity levels and their exact position, overall charge distribution and structure of the energy bands, spin orientation of TM d–electrons and their magnetic interactions, etc.)[7,14,15]. Many of these issues have already been addressed in our previous studies of multi–component II–VI semiconductors doped with magnetic impurities, primarily Mn and Fe[9,10,25,26]. In this paper the studies have been extended to CdSe–based crystalline semiconductors doped with Co. Compared to Mn and Fe, Co as a magnetic impurity in II–VI semiconductors is distinguished by particularly strong d–d interaction and strong sp–d exchange interaction with the conduction band carriers[27]. In order to establish the structural and electronic consequences of Co incorporation into the CdSe crystal lattice, as well as to investigate the possibility of adjusting the material properties by replacing Se with S(Te), we have studied multi–component systems $Cd_{0.98}Co_{0.02}Se$, $Cd_{0.98}Co_{0.02}Se_{0.9}S_{0.1}$ and $Cd_{0.98}Co_{0.02}Se_{0.9}Te_{0.1}$. A comprehensive insight into electronic and local structure of these systems is obtained by means of X–ray absorption fine structure (XAFS) measurements and electronic structure calculations. Important structural information on bond lengths and disorder parameters were extracted from the extended region of the absorption spectra (EXAFS). The near–edge spectral region is, in addition to symmetry of the absorbing atom and its oxidation state, strongly sensitive to structural distortions, orbital hybridization and exchange or loss of atoms. Special attention is, therefore, paid to the analysis of X–ray absorption near edge structure (XANES), in particular to the influence of various structural defects (substitutional impurities, antisite defects, vacancies, interstitials) on local electronic properties, charge transfer and atomic interactions. The extraction of structural and electronic information from XANES spectrum is rather challenging, due to multiple scattering of the photoelectron which dominates this spectral region[28]. Usual strategies for XANES analysis comprise qualitative or (semi)quantitative assessment, when the unknown spectrum is compared with the spectra of reference compounds/theoretical simulations[29], or fitted with linear combination of the known spectra[30]. More advanced strategy comprises simulation of XANES spectra from density functional theory (DFT) optimized structures[26]. In the present work, we utilized theoretical modeling of X–ray absorption near edge structure (XANES) and calculations of local density of electronic states (LDOS). This approach enables to establish relations between the local structures and electronic properties from the characteristic features appearing in the experimental XANES spectra, offering that way possible means for improvement and extension of the practical application of CdSe–based materials by adjusting the details of their electronic structure.

2. Experiment and Theoretical Calculations

Crystalline samples $Cd_{0.98}Co_{0.02}Se$, $Cd_{0.98}Co_{0.02}Se_{0.9}S_{0.1}$, $Cd_{0.98}Co_{0.02}Se_{0.9}Te_{0.1}$ and $Cd_{0.99}Co_{0.01}Se_{0.9}Te_{0.1}$ were grown by the Bridgman method at the Institute of Physics of the Polish Academy of Science (Warszawa, Poland). X–ray diffraction (XRD) measurements were conducted at the Institute of Nuclear Sciences ”Vinča“ of the University of Belgrade (Serbia), using PHILIPS 1050 diffractometer (40 kV and 20 mA) with Ni filtered Cu $K\alpha_{1,2}$ radiation in the Bragg–Brentano geometry, in the range of angles $15^0<2\theta<120^0$, step 0.02^0 and exposure time 0.5 s/step. Cobalt and Se K–edge XAFS spectra were collected at the HASYLAB C1 beamline of Deutsches Elektronen–Synchrotron DESY (Hamburg, Germany). The double crystal monochromator had two crystal pairs mounted on one rotation axis. Achievable Bragg angles ranged from 5^0 to 55.5^0 resulting in a total energy range 2.3 keV ≤ E ≤ 43.4 keV by using Si(111)/Si(311) crystal sets31). Samples were oriented at 45^0 to the incident beam and a 7–segment Ge–detector was used to collect the spectra in the fluorescence yield mode at T=77 K. Multiple scans were taken to improve signal–to–noise ratio. The XAFS data processing and analysis were performed using ATHENA and ARTEMIS packages32) according to the standard procedure described elsewhere33). The following parameters were varied during the fitting: the mean distance of the j–th shell (r_j), the number of atoms in the j–th shell (N_j), the mean–squared displacement of atoms in the j–the shell (σ_j^2) and the edge shift correction (ΔE_0). The stability of each particular fit was tested by changing the k–weights of the EXAFS function $\chi(k)$.

Theoretical modelling of Co and Se K–edge XANES spectra and calculations of local density of electronic states (LDOS) were performed on clusters containing 144 atoms using the GW approach (G refers to one–particle Green’s function and W to screened Coulomb interaction), as implemented in the FEFF 9.03 code34). The scattering potential was determined by self–consistent field (SCF) calculations using the Hedin–Lundqvist exchange–correlation functional. The discontinuities of the potential at the muffin–tin spheres were smoothed using the automatic overlap (AFOLP), and the electric quadrupole transitions were accounted for using the MULTIPOLE card. The effects of the X–ray radiation screening and the photoelectron – core–hole interaction were neglected. The input files were generated by ATOMS software35) according to the relevant crystallographic parameters and sample–specific stoichiometry. The possibility that various native defects (vacancies, interstitials, antisite defects) may exist in the immediate vicinity of the absorbing atom (Se or Co) has also been considered. To account for the experimental resolution and the intrinsic broadening of the experimental spectra due to the finite lifetime of the core–hole, the theoretical XANES spectra were convoluted with a Gaussian function of constant width 0.3 eV, which provided the best agreement with the experimental spectra.

3. Results and Discussion

The XRD patterns of the investigated samples are shown in Fig. 1. All diffraction peaks are readily indexed with the hexagonal wurtzite (WZ) structure (JCPDS card No.08–459) of the host CdSe compound. The WZ structure has C_{3v} symmetry, which can be represented by two interpenetrating hexagonal close–packed anion and cation sublattices displaced relative to each other by approximately $3c/8$. Each atom's nearest neighbourhood (NN) consists of four atoms of different kind, and the next nearest neighbourhood (NNN) has twelve atoms of the same kind. Structural parameters obtained by the XRD data analysis are presented in Table I. Some data of the constituent elements useful for discussion are given in Table II. The lattice constants *a* and *c* (see Table I), change with the radius of substitutional atom(s) (see Table II). Introduction of 2 at.% Co reduces CdSe lattice constant for ~ 0.4 %, co–doping with 10 at. % S reduces the lattice constant for ~ 0.7 %, while co–doping with 10 at. % Te induces lattice expansion for ~ 0.2 %. The investigated samples have nearly identical parameters *u* and their *c/a* ratios are very close to ideal WZ structure39) c/a =1.612 (see Table I), which implies that all impurities occupy regular CdSe lattice sites and induce isotropic structural deformations. Proximity to the ideal *c*/*a* ratio also implies that the symmetry of NN coordination is very close to the tetrahedral (T_d) symmetry, and as such it should be reflected in the X – ray absorption spectra40).

3.1 XANES spectra

Cobalt K–edge XANES spectra of all investigated samples are shown in Fig. 2(a), with the distinctive spectral features labelled *a*–*e*. The spectra of $Cd_{0.98}Co_{0.02}Se$, $Cd_{0.98}Co_{0.02}Se_{0.9}S_{0.1}$ and $Cd_{0.99}Co_{0.01}Se_{0.9}Te_{0.1}$ samples look very much alike. The $Cd_{0.99}Co_{0.01}Se_{0.9}Te_{0.1}$ sample, whose spectrum completely differs, is excluded from further considerations, since it is obvious that Co is not incorporated into regular lattice sites and probably forms some kind of (metallic) clusters. The pre–edge feature *a* primarily originates from s→pd dipole transitions to unoccupied pd–hybrid bands, and its absence in metallic cobalt is ascribed to D_{6h} symmetry which hinders p–d orbital mixing$^{18,41)}$. The absorption edge *b*, which generates peak *c* (white–line) and features *d* and *e* in the spectra of $Cd_{0.98}Co_{0.02}Se$ and $Cd_{0.98}Co_{0.02}Se_{0.9}S(Te)_{0.1}$ samples, are predominantly determined by electric dipole transitions from Co 1s–state to empty p–like states above the Fermi level (E_F)$^{18)}$. The area under the white–line, which is directly proportional to the density of p–holes in the conduction band (CB), is highest in the spectrum of $Cd_{0.98}Co_{0.02}Se$ sample. The spectra of $Cd_{0.98}Co_{0.02}Se_{0.9}S(Te)_{0.1}$ samples have lower white–line and more intense pre–edge structure (see inset of Fig. 2(a)), which indicates higher degree of p–d orbital mixing and possibly larger disorder at the Co site.

Electronic and structural consequences of Co incorporation into CdSe lattice were examined in more detail by theoretical modelling of its K–edge XANES spectra and calculations of local density of electronic states (LDOS). Selected results are presented in Figs. 2(b) and 2(c). Cobalt is treated as a single impurity in CdSe either at regular cation site or at anion antisite. Model $Cd_{(Co)}Se$ with substitutional Co impurity at regular Cd site fairly well reproduces all characteristic features (*a*–*e*) of the experimental spectra, with the feature *b* being somewhat more pronounced (see Fig. 2(b)). Model $CdSe_{(Co)}$ with cobalt at Se antisite generates substantially different spectral shape, and it is therefore excluded from further consideration. The effects of S(Te) co–doping were taken into account by replacing one Se atom from the NN coordination of Co with S(Te). As can be seen in Fig. 2(b), single substitutional S impurity (model $Cd_{(Co)}Se_{(S)}$) does not affect much the overall spectral shape of $Cd_{(Co)}Se$ model spectrum, although it slightly intensifies the pre–edge feature and flattens the feature *b*, which might be an indication that NN environment of Co in $Cd_{0.98}Co_{0.02}Se_{0.9}S_{0.1}$ sample contains S. When instead of

S, the NN Se atom is replaced with Te, the pre–edge completely vanishes (model $Cd_{(Co)}Se_{(Te)}$). Sulphur is likely to intensify the pre–edge structure of the Co K–edge spectrum due to significant overlap between S 3p and Co 3d–states (see Fig. 2(c)), and consequently stronger p–d coupling3,11,14,15,17). In comparison to S 3p orbital, Te 5p orbital has larger radius (it is more dispersed), but its energy is further away from the Co 3d orbital energy (see Table II), so that the disappearance of the pre–edge structure in $Cd_{(Co)}Se_{(Te)}$ model could be related to considerably smaller p–d overlap (see Fig. 2(c)). The fact that the pre–edge structure is clearly visible in the experimental spectrum of $Cd_{0.98}Co_{0.02}Se_{0.9}Te_{0.1}$ (see Fig. 2(a)) implies that the NN environment of Co in this sample does not contain Te, and its higher intensity may be ascribed to larger local distortions induced by Te co–doping (as it will be confirmed by subsequent EXAFS data analysis – see Section 3.2). However, there is no indication of the formation of Te deffect states inside the E_g.

Experimental Se K–edge XANES spectra of the investigated samples are shown in Fig. 3(a), together with the theoretical CdSe spectrum. The shape of the Se K–edge is primarily determined by the multiple–scattering from atoms inside the cluster with radius $r \approx 5$ Å, as determined from the calculations performed on clusters with successive addition of higher atomic shells (not shown), which agrees with earlier reports42). Theoretical model of CdSe XANES spectrum exceptionally well describes the experimental spectra. Comparable positions of multiple–scattering resonances (*a*–*c*) indicate that the tetrahedral coordination around Se remains locally preserved in all investigated samples. Broader features in the experimental spectra indicate higher local disorder43), especially in S(Te) co–doped samples. Closer inspection of the near–edge region reveals the same edge slope in all investigated samples, and a slight shift of the edge position. Also, $Cd_{0.98}Co_{0.02}Se_{0.9}S_{0.1}$ and $Cd_{0.98}Co_{0.02}Se_{0.9}Te_{0.1}$ spectra share almost identical white–line (feature *a*), whose intensity is somewhat lower than in $Cd_{0.98}Co_{0.02}Se$ spectrum (see inset of Fig. 3(a)). To reveal possible causes of these subtle differences in the experimental spectra, theoretical models of Se K–edge XANES spectra, in addition to substitutional impurities, include various native defects44) in the immediate vicinity of the central Se atom. In particular, defects in selenium NN coordination include: isolated Cd vacancy in the basal ab–plane ($V_{Cd(ab)}$) and along the axial direction (V_{Cd}); single Co atom occupying regular Cd site ($Cd_{(Co)}$), Se antisite

($Se_{(Co)}$) and interstitial position (Co_i). Defects in selenium NNN coordination include single substitutional anion impurity (S, Te) and an isolated vacancy (V_{Se}). Selected results of the theoretical modelling are presented in Figs. 3(b)–3(e). As can be seen in Fig. 3(b), models CdSe and CdSe+$V_{Cd(ab)}$ fail to reproduce the absorption edge of the experimental $Cd_{0.98}Co_{0.02}Se$ spectrum. Models CdSe+V_{Cd} and CdSe+V_{Se} are more successful in describing the edge position and slope, but their white–line intensity is reduced below the experimental level. Introduction of Co at several different positions in CdSe (regular cation site, interstitial position and anion antisite) also affects the white–line intensity of the model spectra, as well as the position of the edge and its slope. The best agreement with the experimental $Cd_{0.98}Co_{0.02}Se$ spectrum is achieved when Co replaces Cd at regular lattice site (see Fig. 3(c)), which is in excellent agreement with the Co K–edge XANES results. The model of ideal $Cd_{(Co)}Se$ system therefore served as a basis for S(Te) co–doped systems modelling. Starting from the $Cd_{(Co)}Se$ model and taking into account actual stoichiometry of the samples, $Cd_{(Co)}Se_{(S)}$ and $Cd_{(Co)}Se_{(Te)}$ models were constructed by replacing one out of twelve NNN Se atoms with S(Te) atom. As can be seen in Fig. 3(d), XANES spectra shift toward higher energies as the electronegativity of substituted anions increases$^{45)}$ Te(2.1)<Se(2.55)<S(2.58), leading to stronger and more localized bonds. Since the electrons donated by cations preferentially transfer toward the most electronegative anion in the system$^{46)}$, the position of the band edges and the transition energy of the Se 1s photoelectron change. However, it seems that S(Te) co–doping does not affect much the density of empty Se p–states, which explains why the white–line intensity is still slightly overestimated. If in addition to substitutional S(Te) impurity, NNN Se coordination contains selenium vacancy (V_{Se}), the white–line intensity is reduced to the experimental level in both $Cd_{(Co)}Se_{(S)}$+V_{Se} and $Cd_{(Co)}Se_{(Te)}$+V_{Se} model–systems (see Fig. 3(e)). These results indicate that selenium vacancies may be intrinsic to the investigated samples. Indeed, higher concentration of selenium vacancies in CdSe–based systems is often related to the growth conditions and can be attributed to lower selenium vapour pressure$^{45)}$.

Given that both the threshold energy and density of empty Se p–states are primarily determined by the nearest neighbour interaction (including symmetry allowed sp–d mixing)$^{17,20,47)}$, the observed defect–induced changes of the XANES spectra can be related to LDOS presented in Figs. 4 and 5. Cadmium selenide is a direct bandgap semiconductor and its VB top is predominantly composed of Se p–states, while the CB bottom mostly arises from the Cd s–states with minor contribution of Se s–states$^{14)}$. As can be seen from the calculated CdSe LDOS shown in Fig. 4(a), the energy distribution of various electronic states overlap, as a result of predominantly directional covalent bonding. Selenium p–DOS in the upper part of VB consists of two distinct peaks (see Fig. 4(a)). The first peak (at approximately –6.5 eV) is mainly due to hybridization with Cd s–states, while the second peak (at approximately –4.5 eV) has significant contribution also from the mixed Cd pd–states. The coupling between anion p and Cd d–states reduces cohesive energy and increases the lattice constant, which affects the essential properties of the material, as already mentioned in the Introduction.

In Fig. 4(b), it can be seen that Cd vacancy in the ab–plane ($V_{Cd(ab)}$) primarilly affects sp–hybridization in the VB region below –5 eV, but it has minor impact on Se pDOS near the E_F, which explains its weak influence on the XANES spectrum (see Fig. 3(b)). Cadmium vacancy in the axial direction (V_{Cd}) has a substantial impact on the entire Se pDOS, including the region near the VB top and the CB bottom (see Fig. 4(c)), which is manifested in red shift of the absorption edge (see Fig. 3(b)). This observation is expected given the fact that even in the ideal wurtzite structure (with the ideal c/a ratio) bond along the c–axis is not equivalent to other three NN bonds$^{48)}$. It should be also noted that Cd p–d orbital self–mixing as predicted by CdSe+V_{Cd} model significantly differs from CdSe and CdSe+$V_{Cd(ab)}$ models' predictions (see Fig. 3(a)–(c)), which is yet another reason for differences observed in their XANES spectra$^{49)}$. In the model with an isolated Se vacancy (CdSe+V_{Se}), Cd sDOS becomes more diffuse (see Fig. 4(d)), which primarily affects the electronic structure around the E_F and position of the CB bottom, although the conditions for highly directional bonding are still fulfilled.

Introduction of Co either at interstitial position (see Fig. 4(e)) or at regular cation site (see Fig. 4(f)) induces the profound changes of Se DOS. The electronic structure of VB is significantly altered and the covalent bonding character is locally enhanced. While Cobalt 3d–4s hybrid states interact with the sp–bands of the host CdSe throughout the VB, localized Co d–states pin the E_F position and trigger both inter–atomic (Se–Se) and intra–atomic (Se–Co) p–d orbital mixing, inducing that way additional Se p–state close to the E_F. The models concerning S(Te) co–doping reveal that although both anions (S as deep and Te as shallow impurity)$^{7)}$ are involved in sp–d orbital mixing, they affect the electronic structure and position of the VB top in different ways. According to $Cd_{(Co)}Se_{(S)}$ model, S co–doping enables stronger Co 3d–4s hybridization, which is most prominent in the VB region around –4 eV (see Fig. 4(g)). Besides, Se pDOS in the vicinity of E_F gains intensity upon S→Se substitution due to stronger p–d coupling. Quite the opposite, Se→Te substitution is accompanied by the decrease of Se pDOS intensity near the E_F (see Fig. 4(h)), as a result of weaker p–d coupling. Also, due to anion–specific band offsets$^{7,14,20)}$, empty Se p–states are shifted relatively to $Cd_{(Co)}Se$, so that the charge density at the Se site increases in $Cd_{(Co)}Se_{(S)}$ and decreases in $Cd_{(Co)}Se_{(Te)}$. Selenium vacancy markedly changes electronic structure of the VB (see Figs. 4(i) and 4(j)). The sp–d orbital mixing is significantly reduced and bonding becomes less directional, especially in $Cd_{(Co)}Se_{(S)}+V_{Se}$ (see Fig. 4(i)). However, hybridization between the Co 3d and Se p–states at the E_F remains strong (see Fig. 5(a)), with a significant contribution from Se dDOS (see Fig. 5(b)). Selenium vacancy also leads to nearly the same reduction of density of unoccupied Se p–states in $Cd_{(Co)}Se_{(S)}+V_{Se}$ and $Cd_{(Co)}Se_{(Te)}+V_{Se}$ (see Fig. 5(a)), which can explain similar white line intensities observed in $Cd_{0.98}Co_{0.02}Se_{0.9}S_{0.1}$ and $Cd_{0.98}Co_{0.02}Se_{0.9}Te_{0.1}$ XANES spectra (see Fig. (3)).

Although presented theoretical calculations enabled a valuable qualitative insight into the influence of various structural defects on electronic properties of investigated systems, it should be stressed that the FEFF code is not able to achieve accuracy of the codes based on Density Functional Theory (DFT), expecially when systems with localized 3d electrons are concerned. Relevant DFT–based electronic structure calculations are in progress and will be presented in a separate paper.

3.2 EXAFS spectra

Selenium and Co k–space EXAFS spectra of $Cd_{0.98}Co_{0.02}Se$, $Cd_{0.98}Co_{0.02}Se_{0.9}S_{0.1}$ and $Cd_{0.98}Co_{0.02}Se_{0.9}Te_{0.1}$ samples are presented in Figs. 6(a) and 7(a), and the corresponding Fourier transforms (FT) of the k^2–weighted EXAFS functions $k^2\chi(k)$ in Figs. 6(b) and 7(b). To improve the fit quality, especially the accuracy of bond length determination, the EXAFS data are Fourier transformed to r–space using the longest possible k–space interval. The length of this interval is limited by low amplitude of the backscattering function at high k–values. In addition, the upper limit (k_{max}) of the useful k–data range (Δk) largely depends also on the quality of the investigated sample. The choice of Δk for the Fourier transform window is an important step in the data analysis (if k_{max} is too large, too much noise is added to the Fourier transform). The fits on the same set of data and the same Δk can be compared using a statistical parameter χ_v^2 (reduced chi–square). However, fits on different k–ranges cannot be compared statistically, due to numerous systematics errors (e.g. detector nonlinearity, self–absorption effects, sample inhomogeneity, thickness effects, …).

Structural parameters obtained from the EXAFS data analysis are summarized in Tables III and IV. The fit quality factor was better than 4 % for all reported results. The splitting of the main R–space peak in the Se K–edge EXAFS spectra (see Fig. 6(b)) is due to Ramsauer–Townsend effect$^{50)}$ and corresponds to a minimum of the amplitude envelope in k–space at $k \approx 7$ Å (see Fig. 6(a)). A consistent values of the amplitude reduction factors (S_0^2) have been determined from the $\sigma^2(S_0^2)$ dependences of $k\chi(k)$, $k^2\chi(k)$ and $k^3\chi(k)$ functions$^{33)}$. For each absorbing element (Se and Co) the fits were successively performed with different k–weights (k=1, 2, 3) and S_0^2 fixed from 0.5 to 1.1, with step 0.05. The values S_0^2(Se)=0.7 and S_0^2(Co)=0.67 obtained that way, were used throughout the analysis.

Following the results of XANES data analysis, Co was treated as a substitutional impurity and the EXAFS spectra were fitted accordingly. The NN Se–Co distances obtained from Co and Se K–edges are in excellent agreement (see Tables III and IV), and ideally match the sum of Se and Co tetrahedral covalent radii (see Table II). The Se–Cd and Se–Se distances are consistent with the distances derived from the XRD measurements (see Table III) and also with the results of other studies$^{22,23,51)}$. The Co–Cd distances involve different type of bonding, and therefore they are somewhat shorter (see Table IV). In all investigated samples, cobalt is predominantly surrounded by Se atoms. Tellurium atoms were not found in the first coordination around Co in $Cd_{0.98}Co_{0.02}Se_{0.9}Te_{0.1}$ sample, which indicates that Co–Se pairing is preferential over Co–Te pairing, similarly to Fe–Se preferential pairing in $Zn_{1-x}Fe_xTe_{1-y}Se_y$ system$^{25)}$. In $Cd_{0.98}Co_{0.02}Se_{0.9}S_{0.1}$ sample, however, a small fraction of S ($n \approx 0.1$) was found in the first coordination around cobalt, suggesting the preference for Co–S pairing. Similar tendency for Fe–S pairing has already been established in $Cd_{1-x}Fe_xTe_{1-y}S_y$ system, for even lower concentrations of sulphur[9,10]. The presence of S(Te) induces local distortions of the tetrahedral crystal field at the Co site, and somewhat higher local structural disorder of $Cd_{0.98}Co_{0.02}Se_{0.9}S_{0.1}$ and $Cd_{0.98}Co_{0.02}Se_{0.9}Te_{0.1}$ samples observed in their Co K–edge XANES spectra (see Fig. 2), is reflected in slightly larger parameter σ^2 (see Table IV). Nevertheless, in all investigates samples the interatomic distances determined from the EXAFS data analysis are comparable, which implies that the host CdSe lattice exceptionally well accommodates impurity–induced disorder. The net effect of Co incorporation into Cd site may be explained in terms of their comparable covalent radii and very close d–orbital radii (see Table II). Comparability of Co and Cd radii is a consequence of the proximity of radial distances at which their ground–state electrostatic potential (determined by the overall charge distribution) is equal to the chemical potential. Since the chemical potential of a compound is governed by the electronic charge distribution which accompanies the formation of chemical bonds[52], this means that redistribution of the bonding charge after Co→Cd substitution should not be large. Indeed, preliminary results obtained by the Thomas–Fermi theory[53] indicate that in order for E_F position to be preserved, Co needs to release slightly less electronic charge than Cd, and this can explain the relative ease with which Co can be accomodated in the host CdSe lattice. Still, a full assesment of the doping process requires a detailed consideration of the orbital characteristics of the valence electrons in concern.

4. Conclusions

A comprehensive study of crystalline $Cd_{0.98}Co_{0.02}Se$ and $Cd_{0.98}Co_{0.02}Se_{0.9}S(Te)_{0.1}$ samples by means of Extended X–ray absorption fine structure (EXAFS), X–ray absorption near edge structure (XANES) and electronic structure calculations has enabled a thorough insight into the influence of Co and S(Te) (co)doping on CdSe system, in particular into local structures and electronic features around Co and Se. According to the obtained results, in all investigated samples Co preferably incorporates as a substitution at the cation (Cd) site, while S and Te replace Se at the anion lattice site Cobalt paring preference increases with anion electronegativity due to stronger overlap and more localized bonding electrons. Consequently, a small amount of S atoms has been found in the immediate surrounding of Co, which is not true for Te atoms. Nearest neighbour (NN) and next nearest neighbour (NNN) distances in the S(Te) co–doped systems $Cd_{0.98}Co_{0.02}Se_{0.9}S(Te)_{0.1}$ are close to the corresponding distances in $Cd_{0.98}Co_{0.02}Se$ and their mean–square deviation is rather small. Despite relatively large differences in the size of the substitutional atoms, they all induce isotropic disorder which is exceptionally well accommodated by the host CdSe lattice. Analysis of the electronic structure also suggests that the ease with which Co replaces Cd in the host CdSe lattice results from the fact that their chemical potentials (which regulate the amount of charge involved in bonding) are comparable. We believe that this approach could provide a fairly general method of assessing the compatibility of substitution impurities in a complex system.

Electronic and structural consequences of Co and S(Te) incorporation into the host CdSe lattice and the influence of various structural defects (substitutional impurities, antisite defects, vacancies, interstitials) on local electronic properties, charge transfer and atomic interactions were examined in detail by theoretical modelling of the XANES spectra and calculations of local density of electronic states (LDOS). The most prominent effects that have been revealed are as follows:

- Cobalt impurity at regular cation site induces the most profound changes in the electronic structure of the host CdSe. The entire energy region of chemical interest is affected, especially the part near the band edges. Cobalt d–states pin the Fermi level (E_F) and trigger p–d orbital mixing with anions, which has numerous important consequences on the electronic characteristics of the systems.
- Cadmium vacancy at two different crystallographic positions (in ab–plane and along c–axis) causes entirely different effects, which confirms that these otherwise non–equivalent Cd atoms participate in bonding in rather different ways.
- Selenium vacancies (which are most likely a consequence of low vacuum pressure during the sample growth) affect the electronic structure of the VB and the position of the CB bottom. The sp–d orbital mixing is significantly reduced and bonding becomes less directional.

The presented results have potentially significant implications on the future design and applications of the CdSe–based systems, as they provide better understanding of (co)doping effects and defect–induced changes, which together with a thorough insight into the nature of chemical bonding could help to adjust the details of their electronic structure according to the desired macroscopic characteristics.

Acknowledgment

The research leading to these results is supported by the Serbian Ministry of Education, Science and Technological Development. The authors gratefully acknowledge DESY for providing the beamtime for XAFS experiments.

*E‑mail: iva@vin.bg.ac.rs

1) M.W. Murphy, Y.M. Yiu, M. J. Ward, L. Liu, Y. Hu, J. A. Zapien, Y. Liu, T.K. Sham, J. Appl. Phys. **116**, 193709 (2014).
2) M. Hazra, A. Jana, J. Datta, Appl. Surf. Sci. **454**, 334 (2018).
3) M.J. Watts, T.A.M. Fiducia, B. Sanyal, R. Smith, J.M. Walls, P. Goddard, J. Phys.: Condens. Matter, **32**, 125702 (2020).
4) A. Hu, J. Zhou, P. Zhou, X. Wu, D. Yang, Sol. Energy Mater. Sol. Cells, **214**, 110595 (2020).
5) M. Isshiki, J. Wang, *II–IV Semiconductors for Optoelectronics: CdS, CdSe, CdTe,* in *Springer Handbook of Electronic and Photonic Materials,* eds. S. Kasap, P. Capper, (Springer Handbooks, Springer, Cham, 2017).
6) O. Stroyuk, A. Raevskaya, N. Gaponik, Chem. Soc. Rev. **47**, 5354 (2018).
7) M. J. Caldas, A. Fazzio, A. Zunger, Appl. Phys. Lett. **45**, 671 (1984).
8) C. Ma, X. Gao, T. Wang, R. Chen, Z. Zhu, P. Huo, Y. Liu, Y. Yan, Dalton Trans. **48**, 6824 (2019).
9) N. Bundaleski, I. Radisavljević, N. Ivanović, Z. Rakočević, M. Medić Ilić, N. Romčević, O.M.N.D. Teodoro, Surf. Sci. **681**, 76 (2019).
10) I. Radisavljević, N. Novaković, H.–E. Mahnke, V. Andrić, S. Kurko, D. Milivojević, N. Romčević, N. Ivanović, J. Alloys Compd. **782**, 160 (2019).
11) J. M. Baranowski, J. Phys. C: Solid State Phys. **17**, 6287 (1984).
12) W.A. Harrison, *Elementary Electronic Structure* (World Scientific, Singapore, 1999).
13) S. B. Zhang, S.–H. Wei, A. Zunger, J. Appl. Phys. **83**, 3192 (1998).
14) S.–H. Wei, S.B. Zhang, A. Zunger, J. Appl. Phys. **87**, 1304 (2000).
15) S.–H. Wei, A. Zunger, Phys. Rev. B, **37**, 8958 (1988).
16) T. H. Lee, S. R. Elliott, Adv. Mater. **32**, 2000340 (2020).
17) J. Stankiewicz, F. Palacio, J. Campo, J. Appl. Phys. **75**, 4628 (1994).
18) I. Radisavljević, N. Novaković, B. Matović, N. Paunović, M. Medić, N. Bundaleski, V. Andrić, O.M.N.D. Teodoro, Mater. Res. Bull. **74**, 78 (2016).
19) I. Radisavljević, B. Kuzmanović, N. Novaković, H.–E. Mahnke, LJ. Vulićević, S. Kurko, N. Ivanović, J. Alloys Compd. **697**, 409 (2017).

20) B. Kong, X.–Y. An, T.–X. Zeng, J. Zhang, Phys. Chem. Chem. Phys. **22**, 7474 (2020).

21) S.M. Islam, B.A. Bunker, Phys. Lett. A, **156**, 247 (1991).

22) S.A. Santangelo, E.A. Hinds, V.A. Vlaskin, P.I. Archer, D.R. Gamelin, J. Am. Chem. Soc. **129**, 3973 (2007).

23) P. Fornasini, R. Grisenti, M. Dapiaggi, G. Agostini, T. Miyanaga, J. Chem. Phys. **147**, 044503 (2017).

24) B.V. Robouch, Hao–Hsiung Lin, R.G. Valeev, A.L. Trigub, J. Omar, A. Kisiel, A. Marcelli, J. Alloys Compd. **738**, 218 (2018).

25) I. Radisavljević, J.Trigueiro, N. Bundaleski, M. Medić, N. Romčević, O.M.N.D. Teodoro, M. Mitrić, N. Ivanović, J. Alloys Compd. **632**, 17 (2015).

26) I. Radisavljević, N. Novaković, N. Romčević, M. Mitrić, B. Kuzmanović, S. Bojanić, N. Ivanović, Mat. Chem. Phys. **167**, 236 (2015).

27) H. Alawadhi, I. Miotkowski, A. Lewicki, A. K. Ramdas, S. Miotkowska, M. McElfresh, J. Phys.: Condens. Matter. **14**, 4611 (2002).

28) C.S. Schnohr, M.C. Ridgway, in *X–Ray Absorption Spectroscopy of Semiconductors*, eds. C.S. Schnohr, M.C. Ridgway (Springer–Verlag, Berlin Heidelberg, 2015), p. 7.

29) I. Radisavljević, N. Novaković, N. Ivanović, N. Romčević, M. Manasijević, H.–E. Mahnke, Physica B, **404**, 5032 (2009).

30) I. Radisavljević, N. Novaković, N. Romčević, M. Manasijević, H.–E. Mahnke, N. Ivanović, J. Alloys Compd. **501**, 159 (2010).

31) K. Rickers, W. Drube, H. Schulte–Schrepping, E. Welter, U. Brüggmann, M. Herrmann, J. Heuer, H. Schulz–Ritter, AIP Conf. Proc. **882**, 905 (2007).

32) B. Ravel, M. Newville, J. Synchrotron Rad. **12**, 537 (2005).

33) I. Radisavljević, N. Ivanović, N. Novaković, N. Romčević, M. Mitrić, V. Andrić, H.–E. Mahnke, J. Mater. Sci. **48**, 8084 (2013).

34) A.L. Ankudinov, B. Ravel, J.J. Rehr, S.D. Conradson, Phys. Rev. B, **58**, 7565 (1998).

35) B. Ravel, J. Synchrotron Rad. **8**, 314 (2001).

36) M. Rahm, R. Hoffmann, N.W. Ashcroft, Chem. Eur. J, **22**, 14625 (2016).

37) W. Mönch, *Semiconductor Surfaces and Interfaces, Springer–Verlag* (Berlin Heidelberg, 1995).

38) R. D. Shannon, Acta Cryst. A, **32**, 751 (1976).
39) D. K. Freeman, S. L. Mair, Z. Barnea, Acta Cryst. A¸ **33**, 355 (1977).
40) H.A. Weakliem, D.S. McClure, J. Appl. Phys. **33**, 347 (1962).
41) M. Sano, Inorg. Chem. **27**, 4249 (1988).
42) H. Oyanagi, Z.H. Sun, Y. Jiang, M. Uehara, H. Nakamura, K. Yamashita, L. Zhang, C. Lee, A. Fukano, H. Maeda, J. Synchrotron Rad. **18**, 272 (2011).
43) D.C. Koningsberger, R. Prins, *X–ray absorption: principles, applications, techniques of EXAFS, SEXAFS and XANES* (Wiley–Interscience, Chichester, 1988).
44) D. Bastin, E.V. Lavrov, J. Weber, Phys. Rev. B, **85**, 195204 (2012).
45) W.M. Haynes, *CRC Handbook of Chemistry and Physics: a Ready–reference Book of Chemical and Physical Data* (CRC Press, Boca Raton, 2009).
46) J. Zhou, X. Zhou, X. Sun, M. Murphy, F. Heigl, T.–K. Sham, Z. Ding, Can. J. Chem. **85**, 756 (2007).
47) P. Schröer, P. Krüger, J. Pollmann, Phys. Rev. B, **48**, 18264 (1993).
48) A. P. Sutton, *Electronic Structure of Materials* (Clarendon Press, Oxford, 2004).
49) J.–H. Lee, W.–J. Lee, S.–H. Lee, S. M. Kim, S. Kim, H. M. Jang, Phys. Chem. Chem. Phys. **17**, 7857 (2015).
50) A. G. McKale, B.W. Veal, A.P. Paulikas, S.–K. Chan, G.S. Knapp, Phys. Rev. B, **38**, 10919 (1988).
51) K. Lawniczak–Jablonska, J. Libera , R.J. Iwanowski, J. Alloys Compd. **286**, 89 (1999).
52) P. Politzer, R.G. Parr, D.R. Murphy, J. Chem. Phys. **79**, 3859 (1983).
53) J. P. Solovej, Mol. Phys. **114**, 1036 (2015).

Figure captions

Fig. 1. (Color online) X–ray diffraction patterns of the investigated samples: $Cd_{0.98}Co_{0.02}Se$ (top), $Cd_{0.98}Co_{0.02}Se_{0.9}S_{0.1}$ (middle) and $Cd_{0.98}Co_{0.02}Se_{0.9}Te_{0.1}$ (bottom).

Fig. 2. (Color online) (a) Normalized Co K–edge XANES spectra of $Cd_{0.98}Co_{0.02}Se$ (open circles), $Cd_{0.98}Co_{0.02}Se_{0.9}S_{0.1}$ (full circles), $Cd_{0.98}Co_{0.02}Se_{0.9}Te_{0.1}$ (crossed circles) and $Cd_{0.99}Co_{0.01}Se_{0.9}Te_{0.1}$ (open squares). Inset shows the pre–edge region enlarged; (b) Theoretical Co K–edge XANES spectra of CdSe with Co at regular cation site ($Cd_{(Co)}Se$), Co and S at regular lattice sites ($Cd_{(Co)}Se_{(S)}$), Co at anion antisite ($CdSe_{(Co)}$), Co and Te at regular lattice sites ($Cd_{(Co)}Se_{(Te)}$). Experimental $Cd_{0.98}Co_{0.02}Se$ spectrum with characteristic spectral features labelled *a–e* is given for comparison. Spectra are shifted along the y–axis for clarity. (c) Local density of selected electronic states (LDOS) of $Cd_{(Co)}Se$ (top), $Cd_{(Co)}Se_{(S)}$ (middle) and $Cd_{(Co)}Se_{(Te)}$ (bottom). Corresponding XANES spectra $\mu(E{-}E_0)$ are shown with the dotted line. Vertical line denotes Fermi level (E_F).

Fig. 3. (Color online) (a) Experimental Se K–edge XANES spectra of $Cd_{0.98}Co_{0.02}Se$ (open circles), $Cd_{0.98}Co_{0.02}Se_{0.9}S_{0.1}$ (full circles) and $Cd_{0.98}Co_{0.02}Se_{0.9}Te_{0.1}$ (crossed circles). Theoretical Se K–edge XANES spectrum of CdSe with characteristic features labelled *a–c* is shown on top (solid line). Inset shows the near–edge region of the aligned spectra; (b) Theoretical Se K–edge XANES spectra of CdSe (thin solid line), CdSe with one vacant NN Cd site in the ab–plane ($CdSe+V_{Cd(ab)}$ – dashed line), one vacant NN Cd site along the axial direction ($CdSe+V_{Cd}$ – dotted line), one vacant NNN

Se site (CdSe+V_{Se} – thick solid line); (c) CdSe with Co atom in tetrahedral interstitial position (CdSe+Co_i – thin solid line), Co at regular cation site ($Cd_{(Co)}Se$ – thick solid line), Co at anion antisite ($CdSe_{(Co)}$ – dashed line); (d) CdSe with Co at regular cation site ($Cd_{(Co)}Se$ – dotted line), Co and S at regular lattice sites ($Cd_{(Co)}Se_{(S)}$ – dashed line), Co and Te at regular lattice sites ($Cd_{(Co)}Se_{(Te)}$ – thick solid line); (e) $Cd_{(Co)}Se_{(S)}$ with one vacant NNN Se site ($Cd_{(Co)}Se_{(S)}$+V_{Se} – dashed line), $Cd_{(Co)}Se_{(Te)}$ with one vacant NNN Se site ($Cd_{(Co)}Se_{(Te)}$+V_{Se} – thick solid line). Corresponding experimental spectra are given for comparison in (b)–(e).

Fig. 4. (Color online) Selected LDOS of (a) CdSe, (b) CdSe with one vacant NN Cd site in the ab–plane (CdSe+$V_{Cd(ab)}$), (c) CdSe with one vacant NN Cd site along the axial direction (CdSe+V_{Cd}), (d) CdSe with one vacant NNN Se site (CdSe+V_{Se}), (e) CdSe with one Co atom in tetrahedral interstitial position (CdSe+Co_i), (f) CdSe with one Co atom at regular cation site ($Cd_{(Co)}Se$), (g) CdSe with Co and S atoms at regular lattice sites ($Cd_{(Co)}Se_{(S)}$), (h) CdSe with Co and Te atoms at regular lattice sites ($Cd_{(Co)}Se_{(Te)}$), (i) $Cd_{(Co)}Se_{(S)}$ with one vacant NNN Se site ($Cd_{(Co)}Se_{(S)}$+V_{Se}), (j) $Cd_{(Co)}Se_{(Te)}$ with one vacant NNN Se site ($Cd_{(Co)}Se_{(Te)}$+V_{Se}). Fermi level (E_F) is denoted by vertical line.

Fig. 5. (Color online) Selenium pDOS (a) and dDOS (b) of selected model systems. Fermi level (E_F) is denoted by vertical line.

Fig. 6. (Color online) (a) Selenium K–edge EXAFS spectra of $Cd_{0.98}Co_{0.02}Se$ (top), $Cd_{0.98}Co_{0.02}Se_{0.9}S_{0.1}$ (middle), $Cd_{0.98}Co_{0.02}Se_{0.9}Te_{0.1}$ (bottom); (b) the corresponding Fourier transforms (FT). Experimental data are represented with solid lines and the best

obtained fits with dashed lines. The FT was performed over the k–range: (2.320–10.652) Å^{-1} for sample $Cd_{0.98}Co_{0.02}Se$, (2.379–11.351) Å^{-1} for sample $Cd_{0.98}Co_{0.02}Se_{0.9}S_{0.1}$ and (2.362–10.765) Å^{-1} for sample $Cd_{0.98}Co_{0.02}Se_{0.9}Te_{0.1}$. The contribution of each scattering path is given separately.

Fig. 7. (Color online) (a) Cobalt K–edge EXAFS spectra of $Cd_{0.98}Co_{0.02}Se$ (top), $Cd_{0.98}Co_{0.02}Se_{0.9}S_{0.1}$ (middle), $Cd_{0.98}Co_{0.02}Se_{0.9}Te_{0.1}$ (bottom); (b) the corresponding Fourier transforms (FT). Experimental data are represented with solid lines and the best obtained fits with dashed lines. The FT was performed over the k–range: (2.707–9.623) Å^{-1} for $Cd_{0.98}Co_{0.02}Se$, (2.766–11.732) Å^{-1} for $Cd_{0.98}Co_{0.02}Se_{0.9}S_{0.1}$ and (2.594–10.987) Å^{-1} for $Cd_{0.98}Co_{0.02}Se_{0.9}Te_{0.1}$. The contribution of each scattering path is given separately.

Table I. Structural parameters of the investigated samples obtained by the XRD analysis (*a*, *c* – lattice constants, *u* – internal parameter). CdSe data[36)] are given for comparison. The data are ordered according to ascending lattice constants.

Sample	*a* (Å)	*c* (Å)	*u*	*c/a*
$Cd_{0.98}Co_{0.02}Se_{0.9}S_{0.1}$	4.267	6.958	0.377	1.631
$Cd_{0.98}Co_{0.02}Se$	4.280	6.985	0.377	1.632
CdSe	4.299	7.010	0.376	1.631
$Cd_{0.98}Co_{0.02}Se_{0.9}Te_{0.1}$	4.308	7.034	0.377	1.633

Table II. Some parameters of the elements of interest: r_c – covalent radius37); r_i – ionic radius38) for formal valence two in coordination IV (Co, Cd, Te) and VI (Se, S); r_l – orbital radii (l=p,d); ε_s, ε_p, ε_d – orbital energies; ε_h – sp^3 hybridization energy12).

	r_c (Å)	r_i (Å)	r_l (Å)	ε_s (eV)	ε_p (eV)	ε_d (eV)	ε_h^{sp} (eV)
Co	1.32	0.58	0.696 (3d)	–7.31(4s)	–3.84(4p)	–17.77 (3d)	–
Cd	1.48	0.78	0.693 (4d)	–7.21(5s)	–3.89 (5p)	–20.77 (4d)	–4.72
S	1.04	1.84	10.1 (3p)	−24.01 (3s)	–11.60 (3p)	–	–14.71
Se	1.14	1.98	12.1 (4p)	−22.86 (4s)	–10.68 (4p)	–	–13.73
Te	1.32	2.21	15.9 (5p)	–19.12 (5s)	–9.54 (5p)	–	–11.94

Table III. Structural parameters obtained from the Se K–edge EXAFS data analysis: r–interatomic distance, ΔE_0–edge shift correction, σ^2–mean–square distance variation, The amplitude reduction factor S_0^2 was determined to be 0.70.

Sample	r (Å)		ΔE_0 (eV)	σ^2 (Å^2)
$Cd_{0.98}Co_{0.02}Se$	Se–Cd	2.60(1) #2.616	1.3(6)	0.0015(4)
	Se–Co	2.46(5)	1.3	0.016(8)
	Se–Se	4.27(4) #4.280	0(3)	0.015(3)
$Cd_{0.98}Co_{0.02}Se_{0.9}S_{0.1}$	Se–Cd	2.611(7) #2.61	2.9(6)	0.0016(6)
	Se–Co	2.48(7)	2.9	0.010(9)
	Se–Se	4.31(4) #4.26	3(3)	0.012(3)
$Cd_{0.98}Co_{0.02}Se_{0.9}Te_{0.1}$	Se–Cd	2.64(1) #2.63	2(1)	0.001(1)
	Se–Co	2.48(3)	2	0.001(1)
	Se–Se	4.34(9) #4.30	–0(6)	0.015(6)

#Distances derived from the XRD measurements.

Table IV. Structural parameters obtained from the Co K–edge EXAFS data analysis: r–interatomic distance, ΔE_0–edge shift correction, σ^2–mean–square distance variation. The amplitude reduction factor S_0^2 was determined to be 0.67.

Sample	r (Å)		ΔE_0 (eV)	σ^2 (Å^2)
$Cd_{0.98}Co_{0.02}Se$	Co–Se	2.46(1)	3(3)	0.003(1)
	Co–Cd	4.17(7)	–3(3)	0.015(5)
$Cd_{0.98}Co_{0.02}Se_{0.9}S_{0.1}$	Co–Se	2.45(1)	1(1)	0.002(1)
	Co–Cd	4.18(3)	–1(1)	0.016(3)
$Cd_{0.98}Co_{0.02}Se_{0.9}Te_{0.1}$	Co–Se	4.45(1)	3(1)	0.002(1)
	Co–Cd	4.20(6)	–1(2)	0.019(4)

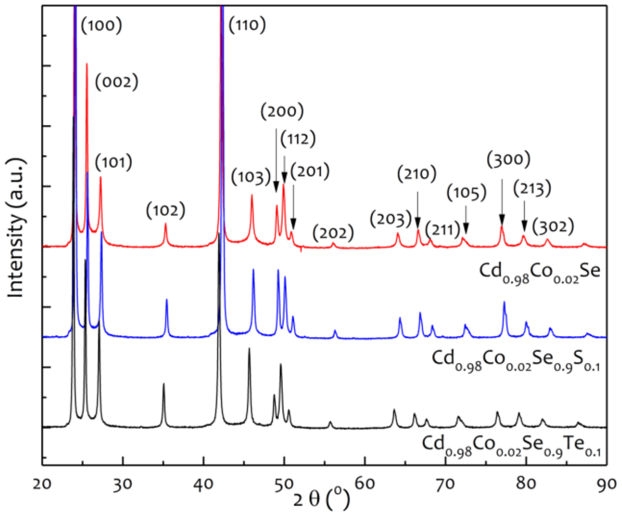
(100)
(110)
(002)
(200)
(112)
(101)
(201)
(210)
(300)
(103)
(105)
(213)
(102)
(203)
(211)
(302)
(202)
Cd0.98Co0.02Se
Cd0.98Co0.02Se0.9S0.1
Cd0.98Co0.02Se0.9Te0.1
Intensity (a.u.)
2 θ (°)
20
30
40
50
60
70
80
90

Fig. 1.

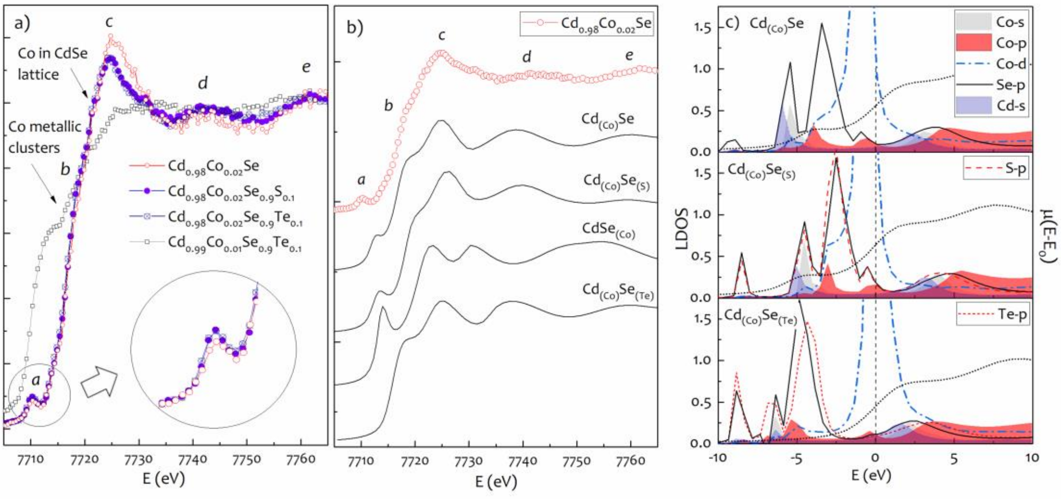
a)
c
Co in CdSe lattice
Co metallic clusters
b
d
e
a
$Cd_{0.98}Co_{0.02}Se$
$Cd_{0.98}Co_{0.02}Se_{0.9}S_{0.1}$
$Cd_{0.98}Co_{0.02}Se_{0.9}Te_{0.1}$
$Cd_{0.99}Co_{0.01}Se_{0.9}Te_{0.1}$
Normalized intensity (a.u.)
7710
7720
7730
7740
7750
7760
E (eV)
b)
$Cd_{0.98}Co_{0.02}Se$
a
b
c
d
e
$Cd_{(Co)}Se$
$Cd_{(Co)}Se_{(S)}$
$CdSe_{(Co)}$
$Cd_{(Co)}Se_{(Te)}$
7710
7720
7730
7740
7750
7760
E (eV)
c)
$Cd_{(Co)}Se$
Co-s
Co-p
Co-d
Se-p
Cd-s
$Cd_{(Co)}Se_{(S)}$
S-p
$Cd_{(Co)}Se_{(Te)}$
Te-p
LDOS
$\mu(E-E_0)$
0.0
0.5
1.0
1.5
-10
-5
0
5
10
E (eV)

Fig. 2.

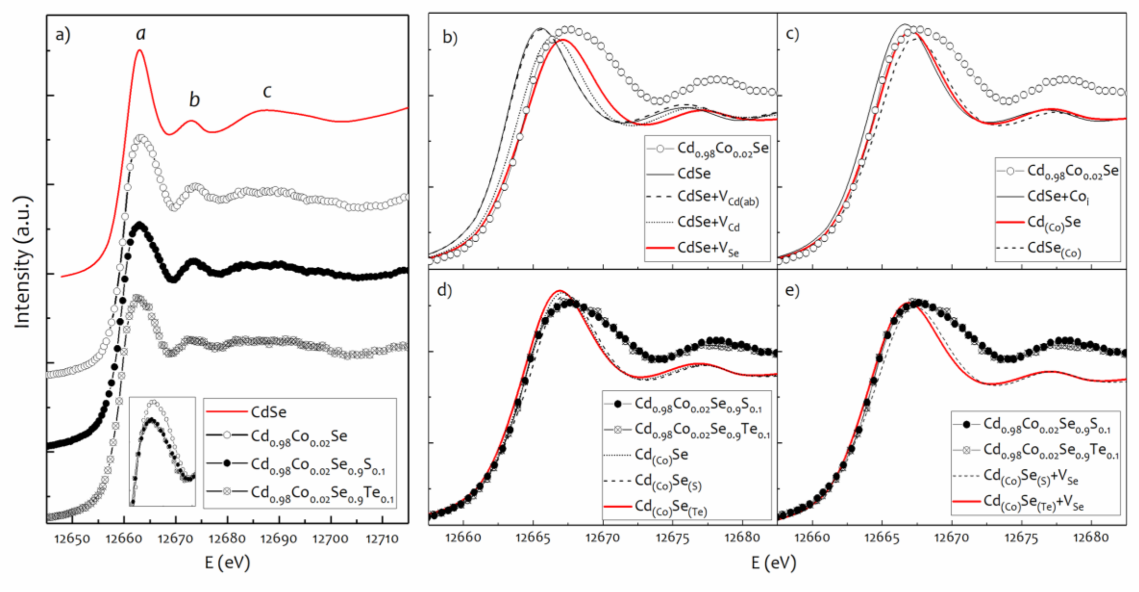
a)
a
b
c
Intensity (a.u.)
12650
12660
12670
12680
12690
12700
12710
E (eV)
CdSe
$Cd_{0.98}Co_{0.02}Se$
$Cd_{0.98}Co_{0.02}Se_{0.9}S_{0.1}$
$Cd_{0.98}Co_{0.02}Se_{0.9}Te_{0.1}$
b)
$Cd_{0.98}Co_{0.02}Se$
CdSe
$CdSe+V_{Cd(ab)}$
$CdSe+V_{Cd}$
$CdSe+V_{Se}$
c)
$Cd_{0.98}Co_{0.02}Se$
$CdSe+Co_{i}$
$Cd_{(Co)}Se$
$CdSe_{(Co)}$
d)
$Cd_{0.98}Co_{0.02}Se_{0.9}S_{0.1}$
$Cd_{0.98}Co_{0.02}Se_{0.9}Te_{0.1}$
$Cd_{(Co)}Se$
$Cd_{(Co)}Se_{(S)}$
$Cd_{(Co)}Se_{(Te)}$
e)
$Cd_{0.98}Co_{0.02}Se_{0.9}S_{0.1}$
$Cd_{0.98}Co_{0.02}Se_{0.9}Te_{0.1}$
$Cd_{(Co)}Se_{(S)}+V_{Se}$
$Cd_{(Co)}Se_{(Te)}+V_{Se}$
12660
12665
12670
12675
12680
12660
12665
12670
12675
12680
E (eV)

Fig. 3.

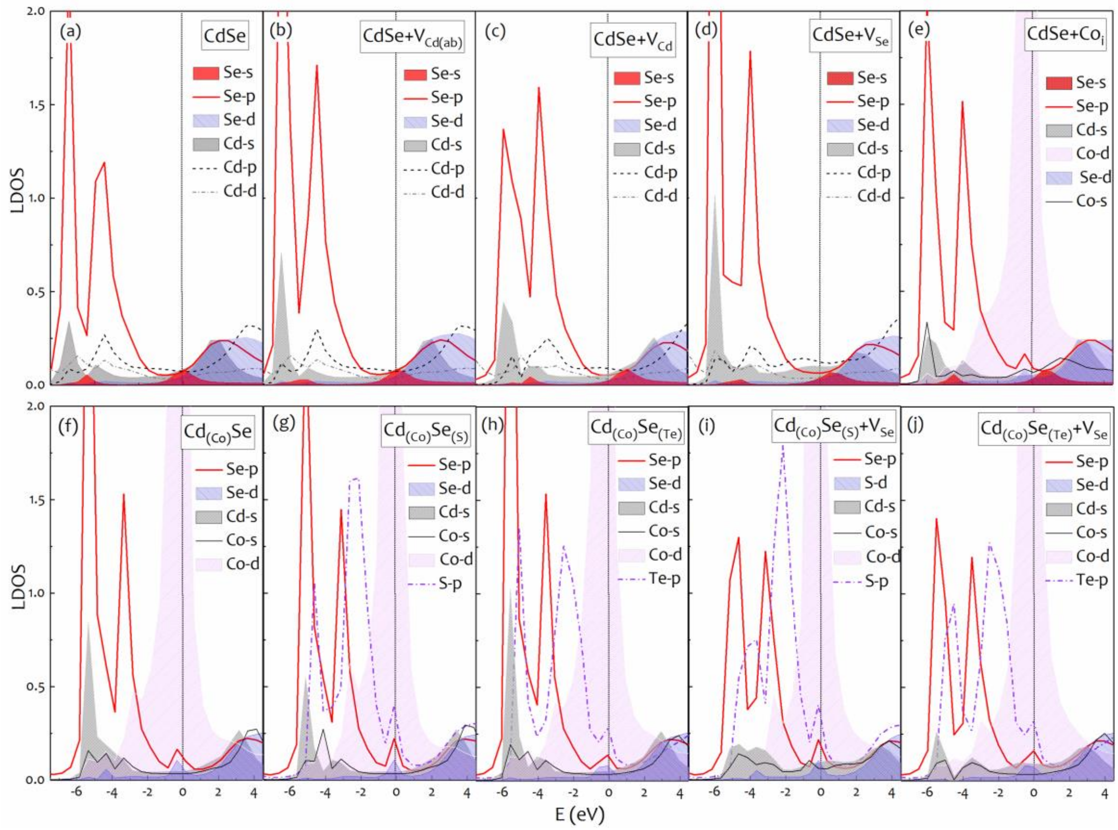

(a) CdSe
(b) CdSe+V$_{Cd(ab)}$
(c) CdSe+V$_{Cd}$
(d) CdSe+V$_{Se}$
(e) CdSe+Co$_i$
(f) Cd$_{(Co)}$Se
(g) Cd$_{(Co)}$Se$_{(S)}$
(h) Cd$_{(Co)}$Se$_{(Te)}$
(i) Cd$_{(Co)}$Se$_{(S)}$+V$_{Se}$
(j) Cd$_{(Co)}$Se$_{(Te)}$+V$_{Se}$
Se-s
Se-p
Se-d
Cd-s
Cd-p
Cd-d
Co-d
Co-s
S-d
S-p
Te-p
LDOS
0.0
0.5
1.0
1.5
2.0
-6
-4
-2
0
2
4
E (eV)

Fig. 4.

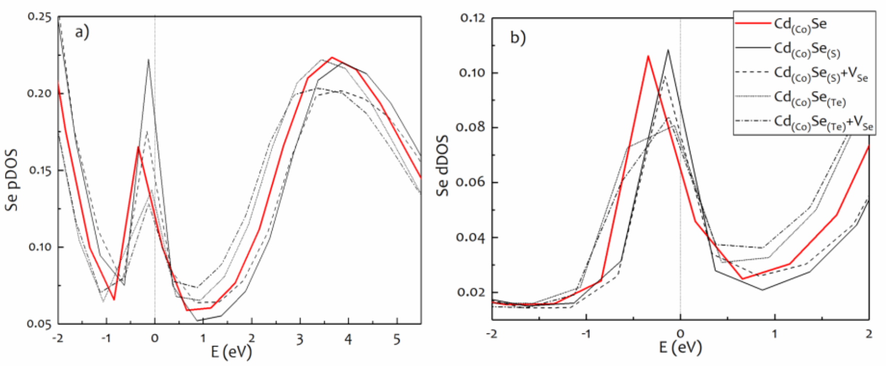
a)
Se pDOS
0.25
0.20
0.15
0.10
0.05
-2
-1
0
1
2
3
4
5
E (eV)
b)
Se dDOS
0.12
0.10
0.08
0.06
0.04
0.02
-2
-1
0
1
2
E (eV)
$Cd_{(Co)}Se$
$Cd_{(Co)}Se_{(S)}$
$Cd_{(Co)}Se_{(S)}+V_{Se}$
$Cd_{(Co)}Se_{(Te)}$
$Cd_{(Co)}Se_{(Te)}+V_{Se}$

Fig. 5.

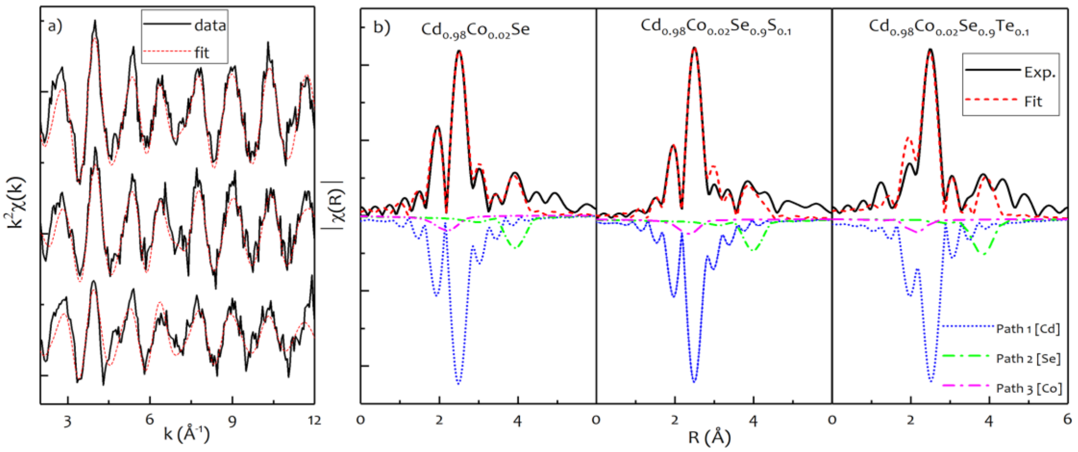
a)
data
fit
$k^2\chi(k)$
3
6
9
12
k (Å^{-1})
b)
$Cd_{0.98}Co_{0.02}Se$
$Cd_{0.98}Co_{0.02}Se_{0.9}S_{0.1}$
$Cd_{0.98}Co_{0.02}Se_{0.9}Te_{0.1}$
$|\chi(R)|$
Exp.
Fit
Path 1 [Cd]
Path 2 [Se]
Path 3 [Co]
0
2
4
6
R (Å)

Fig. 6.

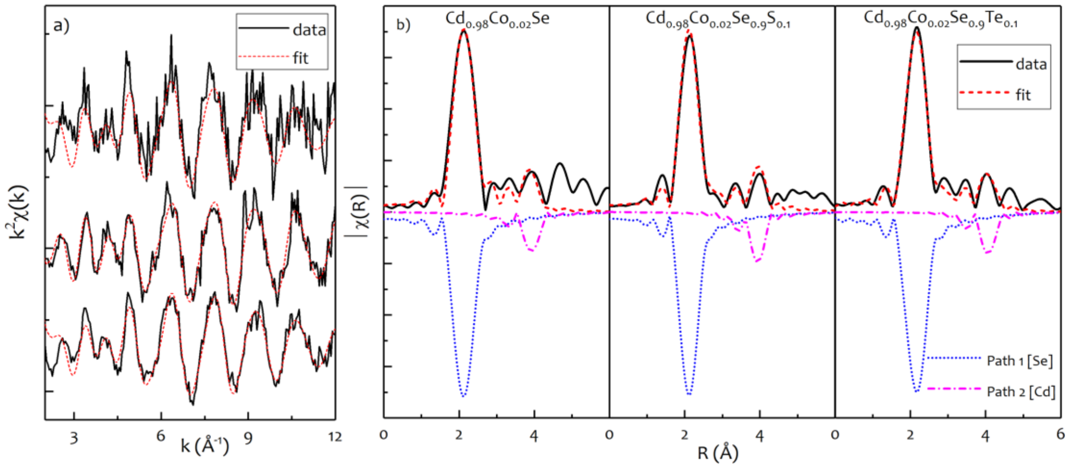
a)
data
fit
k²χ(k)
3
6
9
12
k (Å⁻¹)
b)
Cd0.98Co0.02Se
Cd0.98Co0.02Se0.9S0.1
Cd0.98Co0.02Se0.9Te0.1
data
fit
Path 1 [Se]
Path 2 [Cd]
|χ(R)|
0
2
4
0
2
4
0
2
4
6
R (Å)

Fig. 7.